

Conveyor-mode electron shuttling through a T-junction in Si/SiGe

Max Beer ,¹ Ran Xue,¹ Lennart Deda,¹ Stefan Trellenkamp,² Jhii-Sian Tu,² Paul Surrey,¹ Inga Seidler,¹ Hendrik Bluhm,^{1,3} and Lars R. Schreiber ,^{1,*}

¹ JARA-FIT Institute for Quantum Information, Forschungszentrum Jülich GmbH and RWTH Aachen University, 52074 Aachen, Germany

² Helmholtz Nano Facility (HNF), Forschungszentrum Jülich, Jülich, Germany

³ ARQUE Systems GmbH, 52074 Aachen, Germany

Conveyor-mode shuttling in gated Si/SiGe devices enables adiabatic transfer of single electrons, electron patterns and spin qubits confined in quantum dots across several microns with a scalable number of signal lines. To realize their full potential, linear shuttle lanes must connect into a two-dimensional grid with controllable routing. We introduce a T-junction device linking two independently driven shuttle lanes. Electron routing across the junction requires no extra control lines beyond the four channels per conveyor belt. We measure an inter-lane charge transfer fidelity of $F = 100.0000000^{+0}_{-9 \times 10^{-7}} \%$ at an instantaneous electron velocity of 270 mm s^{-1} . The filling of 54 quantum dots is controlled by simple atomic pulses, allowing us to swap electron patterns, laying the groundwork for a native spin-qubit SWAP gate. This T-junction establishes a path towards scalable, two-dimensional quantum computing architectures with flexible spin qubit routing for quantum error correction.

Electron and hole spin quantum computing in electrostatically defined SiGe quantum dots (QDs) have progressed considerably [1]: Single- and two-qubit gate fidelities exceeding the error correction threshold [2–5] as well as scaling of multi-qubit devices up to twelve qubits [6] have been demonstrated. These scaling efforts manifest as increasingly large (bi-) linear [6–9] and dense, two-dimensional QD arrays [10, 11]. Such dense architectures as well as large linear arrays suffer from limited scalability due to wiring bottlenecks and difficulties in implementing the long-range qubit coupling required [12, 13], while two-dimensional qubit topologies with millions of physical qubits are needed for the implementation of many efficient quantum error correction algorithms [14, 15].

To solve these challenges, qubit shuttling has been investigated intensely. The two dominant methods of qubit shuttling in QDs are bucket-brigade [16–19] and conveyor-mode [19–23] shuttling. The latter features higher spin shuttle fidelity and has been demonstrated as the more scalable solution [19, 21, 22, 24, 25] as it demands only a small and constant number of control lines and signals independent of the shuttling distance [26–28]. However, the required extension of conveyor-mode shuttling of qubits into two dimensions has not been demonstrated so far. Shuttle junctions and qubit routing pose a challenge even for other, arguably more mature qubit platforms [29–31]. Surface-code quantum error correction for spin-qubits requires thousands of physical qubits to encode one logical qubit thus millions of single electron spins need to be positioned and controlled. This sets high demands on the fidelity for controlling these electrons, while control signals must be simple to co-integrate signal generation and routing on the chip [13, 27].

Here we demonstrate a key building block, a two-dimensional intersection of orthogonal one-dimensional

conveyor-belt shuttle lanes. This T-junction consists of 54 QDs and enables flexible routing of single electrons. Despite its gate design complexity, all routing and filling of all QDs is controlled by only eight simple voltage signals. We observe single electron transport across the $10 \mu\text{m} \times 5 \mu\text{m}$ device with an inter-lane charge transfer fidelity of $F = 100.0000000^{+0}_{-9 \times 10^{-7}} \%$ at an instantaneous electron velocity of 270 mm s^{-1} . We demonstrate the first step towards a spin-SWAP gate native to our device topology by permuting initialized QD fillings also referred to as electron patterns [21].

T-JUNCTION DEVICE AND ATOMIC PULSES

The T-junction is composed of two individual QuBus shuttle lanes, labeled x-shuttle and y-shuttle, joined at a 90° angle with a single electron transistor (SET) formed at the exterior-facing end of each lane (Fig. 1a). Electrostatic gates used in the operation of the device are labeled in Fig. 1a. The large number of gates and device terminals allows for more flexibility and fine control over the electron confinement potential than actually required to operate the device in this work. For this reason, gates are grouped in connected gate sets $S_{j,i}$ ($i \in \{1, 2, 3, 4\}$, $j \in \{\text{x}, \text{y}\}$) as indicated by color in Fig. 1a (see methods for details). The same voltage is applied to each gate in a set, significantly reducing the effective number of terminals required to operate the T-junction.

We define a pulse P as time-dependent voltage sequences simultaneously applied to a few gate sets (in addition to a constant DC voltage, details on notation in methods). A pulse that is not composed of other pulses is called an atomic pulse, of which we define eight (1 and 0 electron loading L_1 , L_0 ; charge readout R_{CC} and preparation $\lambda_{\text{L} \rightarrow \text{R}}$ (Fig. 1b); linear charge shuttling λ_{x}^1 , λ_{y}^1 (Fig. 1c); T-junction transfers λ_{JR}^1 , λ_{JL}^1 (Fig. 1d)), each achieving a specific function explained below or in

* lars.schreiber@physik.rwth-aachen.de

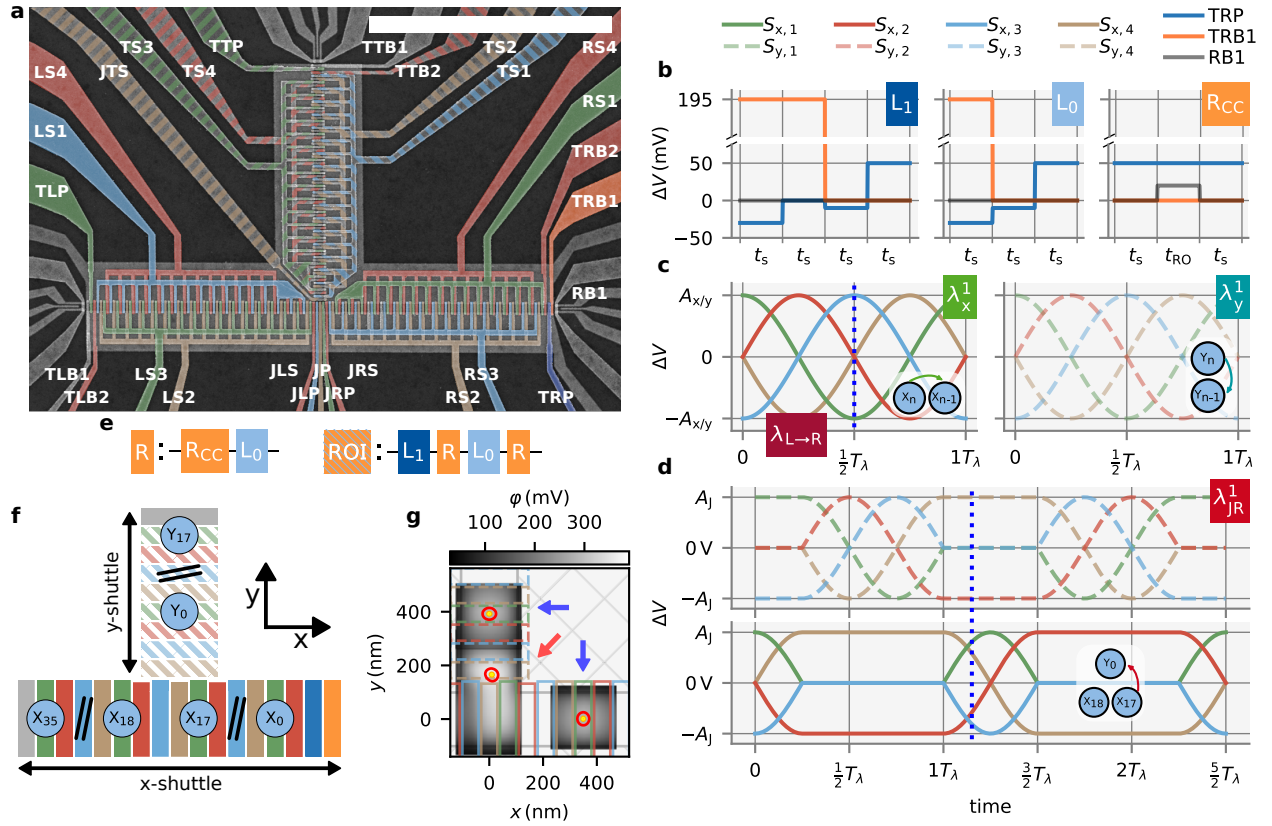


Fig. 1. T-junction device and atomic pulses. **a** False color scanning electron micrograph of the surface of a device nominally identical to the device measured, including gate labels. Gate color coding is consistent between all sub-figures and indicates gates comprising gate sets $S_{x,i}$ and $S_{y,i}$ (see methods). The scale bar is 5 μm . **b** Atomic pulses for charge initialization and readout. The indicated voltages are typical values. Typical values are $t_S \approx 10$ ms and $t_{RO} \approx 100$ ms. **c** Horizontal and vertical charge shuttle atomic pulses. The first half of λ_x^1 , up to the dashed line, describes $\lambda_{L \rightarrow R}$. **d** Junction transfer atomic pulse. Pulses for finger gates in x- and y-shuttle are shown on the bottom and top, respectively. Note that the x- and y-shuttle are not operated simultaneously. **e** Commonly used composite pulses. R: destructive readout pulse. ROI: readout and initialization calibration pulse. **f** Nominal dot positions in the idle state. In the readout state (see methods), all QD X_n are shifted two gates towards the right. Periodic continuation of more QDs are omitted but indicated with (//) symbols. **g** Simulated potentials φ and electron ground state probability densities (yellow-red circular shapes) at three positions in the device corresponding to three points in time. Claviature gates are shown as outlines and screening gates are indicated as a light gray grid. Blue arrows: Electron states in QD X_{16} and QD Y_0 in the idle state. Red arrow: Electron during inter-lane junction transfer, time indicated by blue dashed line in (d). 95 %, 68 %, 1 % probability density levels shown in yellow, orange and red, respectively. (time-dependence of simulations in Supplementary Movies 1 and 2)

methods. We abbreviate often used pulses related to initialization and readout by R and ROI (Fig. 1e). In total, only eleven voltage channels are required to apply all atomic pulses. Despite the device complexity, these eight atomic pulses are sufficient to operate the entire device.

Typical for the conveyor-belt shuttling approach [20, 21, 26, 27], QDs are formed under every fourth gate in the x- and y-shuttle lane, here in total 54 – labeled QD X_i and QD Y_i (Fig. 1f). Forward conveyor-belt shuttling in the x-(y-)shuttle lane means a continuous transfer of a QD positioned at QD X_n to QD X_{n-1} (QD Y_n to QD Y_{n-1}). To facilitate forward conveyor-belt shuttling, shuttle gates in the x- and y-shuttle are pulsed by the

voltage

$$\Delta V_{g \in S_{j,i}}(t) = A_j \sin\left(-\frac{2\pi t}{T_\lambda} + i \cdot \frac{\pi}{2}\right) \quad i \in \{1, 2, 3, 4\} \quad j \in \{x, y\}$$

where T_λ is the shuttle period and A_x , A_y are the drive amplitudes for the x- and y-shuttle, respectively. The voltage pulses applied to $S_{x,3}$ are also applied to TRP. A single period T_λ of this sequence, applied to either the x- or y-shuttle, defines atomic pulses λ_x^1 or λ_y^1 (Fig. 1c), continuously moving a QD a distance of four gates, i.e. $\lambda = 280$ nm with an instantaneous shuttle velocity $v_\lambda = \lambda/T_\lambda$.

The atomic pulse λ_{JR}^1 is specific to the T-junction and transfers the charge occupancy from QD X_{17} continuously into QD Y_0 (finite-element simulation in Fig.

1g with details in Supplementary Note I). The transfer is realized by coordinated conveyor-mode shuttling with a drive amplitude A_J and velocity v_J in the x- and y-shuttle. It includes halting and reversing both shuttle lanes appropriately at $T_\lambda/4$ intervals (Fig. 1d), but otherwise signal bandwidth requirements are similar to λ_x^1 and λ_y^1 . The analogue atomic pulse transferring the charge occupancy directly from QD X_{18} into QD Y_0 , λ_{JL}^1 , is additionally defined, differing only by the distance and direction of conveyor-mode shuttling in the x-shuttle (Extended Data Fig. 1).

SINGLE ELECTRON SHUTTLING

This work focuses on shuttling and routing across a T-junction. Because no charge sensor is implemented directly at the densely gated center of the T-junction, we investigate the initial success of routing across the T-junction by continuing to linearly shuttle in the x-(y-)shuttle, until the shuttled charge encounters the left (upper) end of the x-(y-)shuttle lane, which can be detected [21]. Then, we amplify the inter-lane junction transfer infidelity by repeatedly looping around the T-junction with a single electron.

First we verify shuttling in the x-shuttle lane and thus shuttle straight through the T-junction. The pulse (Fig. 2a with $A_x = 260$ mV and $v_\lambda = 270$ mm s $^{-1}$) shuttles the initialized charge from QD X_0 into QD X_n , followed by readout of QD X_0 to verify that the charge was shuttled away and finally returns it to QD X_0 , shuttling for three periods more than required to return the charge. With in total seven readouts (three shuttling periods each before and after the charge is expected to return), we detect unexpectedly advanced or delayed charge. These readouts are labeled in the resulting data by their Δn value, which is $\Delta n = n$ for the first readout, when the charge is expected to be farthest from the SET and $\Delta n \in [-3, 3]$, indicating the readouts relative to the expected $\Delta n = 0$ readout ($\Delta n > 0$ and $\Delta n < 0$ corresponding to advanced or delayed charge, respectively). This pulse is applied with zero electrons loaded as a reference and then, immediately afterwards, with one electron to ensure the measured electron occupancy is only a consequence of the deliberate initialization of QD X_0 . A shuttle event is called successful, if the charge is detected only at $\Delta n = 0$ and no charge is detected during the reference sequence. By a modified pulse (Fig. 2b), we verify turning within the T-junction by inter-lane junction transfer ($v_J = v_\lambda$, $A_J = A_x = A_y$), shuttling until QD Y_n .

When initializing QD X_0 with one electron, that electron is observed as expected in readout $\Delta n = 0$ when attempting to shuttle for $n \in \{4, 35\}$ ($n \in \{4, 17\}$ for turning) during almost all repetitions (Fig. 2a,b). No electrons are detected if zero electrons are loaded, as expected. For $n = 36$ ($n = 18$ for turning), far fewer electrons are detected in readout $\Delta n = 0$, while many electrons are detected earlier in readouts $\Delta n \in \{1, 2, 3\}$.

This is our fingerprint that the electron actually reaches the end of the x-(y-)shuttle lane at which a large barrier is formed by gate TLB1 (TTB1) scattering the electron across neighboring QDs. Hence, it demonstrates that we routed a single charge across the T-junction. We evaluate the pulse fidelity F_{total} as defined in methods (results noted in Table 1). The charge control in the T-junction is reliable across 1000 repetitions and independent of shuttled distance – we only observe one unsuccessful shuttle event for $v_\lambda = 28$ mm s $^{-1}$ and 270 mm s $^{-1}$. A deviation of F_{total} from 100 % could not be determined as the duration of the pulses is limited by initialization and readout (L_0 , L_1 and R_{CC}).

When shuttling in the junction, three main shuttle paths exist, each with its own range of possible drive amplitudes and shuttle velocities. To explore the optimal parameter (A_J, v_J) space for operation of the T-junction, we apply several pulses that first shuttle the initialized QD close to the junction using the good drive amplitudes $A_x = A_y = 260$ mV and shuttle velocity $v_\lambda = 270$ mm s $^{-1}$ and then either route the initialized QD into the y-shuttle lane using λ_{JR}^1 or λ_{JL}^1 or shuttle from QD X_{16} to QD X_{18} using λ_x^{-2} , while varying the drive amplitude A_J at shuttle velocity v_J (Fig. 3a). Note that we set $A_x = A_J$ and $v_\lambda = v_J$ for the final path when shuttling from QD X_{16} to QD X_{18} only. The full pulses used here are shown in Extended Data Fig. 3. The pulse fidelities observed remain close to 100 % for $A_J \geq 133$ mV for λ_{JR}^1 , λ_{JL}^1 and λ_x^{-2} , with only a minor dependence of the minimum reliable drive amplitude on the instantaneous shuttle velocity during junction transfer shuttling v_J . While the cable bandwidth limits the investigated v_J to one order of magnitude lower than required for spin-coherent shuttling [26], we observe no significant reduction of pulse fidelity up to the maximum possible v_J . The drive amplitudes allowing for successful inter-lane junction transfer shuttling are similar to the required drive amplitude for linear shuttling in Ref. [21], performed on a different device design, albeit on a nominally identical heterostructure.

CHARGE LOOPING WITHIN THE T-JUNCTION

As the previous pulses transfer the initialized charge through the junction only two times per pulse, we expect their fidelity to be dominated by charge state preparation and readout (SPAM) errors and possibly by errors occurring when shuttling along the x- and y-shuttle lanes. Additionally, charge initialization and readout contribute the majority of measurement time, thereby limiting the total number of repetitions. Hence, these pulses are not able to resolve the small infidelity of inter-lane junction transfer ($\lambda_{JR}^{\pm 1}$ and $\lambda_{JL}^{\pm 1}$) at the center of the T-junction. We therefore modify the pulse such that the initialized charge is instead shuttled into QD X_{16} using again the known good drive amplitudes $A_x = A_y = 260$ mV. Then, we loop the charge n_{loops} -times within the T-junction,

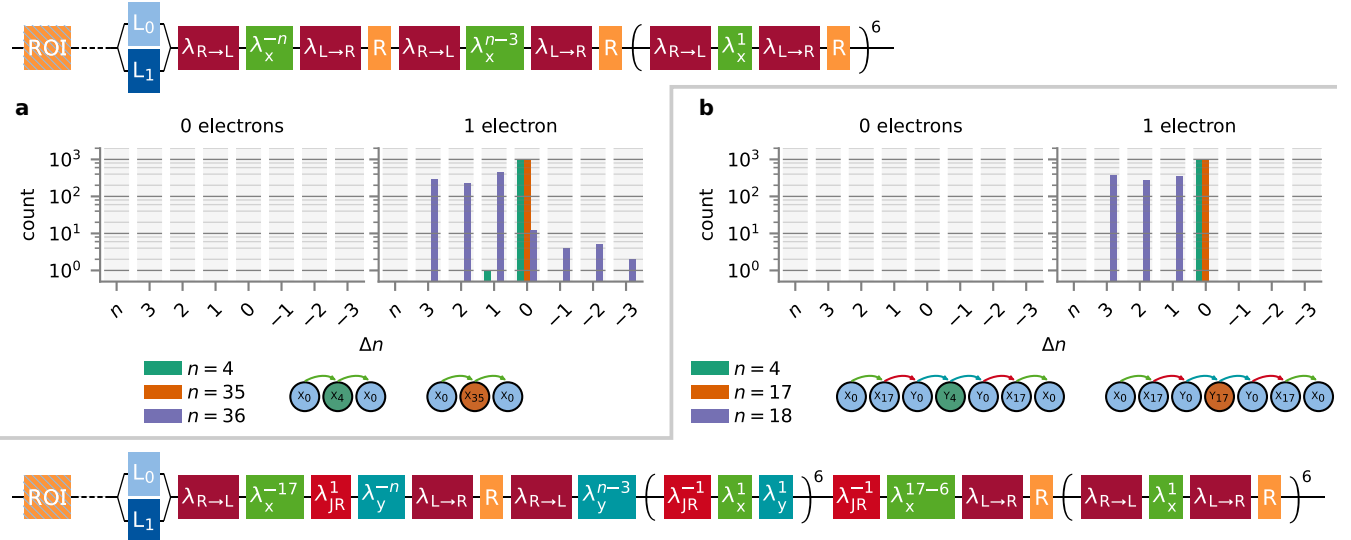


Fig. 2. Verifying shuttling in the x- and y-shuttles. Applied pulses and readout histograms with one and zero electrons loaded, the latter as reference pulse. Branching notation in the pulses indicate that the whole pulse is repeated once for each branch, with the exception of the ROI-pulse separated by dashed lines, which is only performed for the first branch repetition. Histograms show the sum of QD X_0 occupancy readout counts separated for the pulse branches with either one electron or zero electrons loaded. The QDs along the shuttle paths are shown next to the legends. $n_{\text{total}} = 1000$, $A_x = A_y = A_J = 260$ mV and $v_\lambda = v_J = 270$ mm s $^{-1}$ for all measurements. Results for $v_\lambda = v_J = 28$ mm s $^{-1}$ shown in Extended Data Fig. 2. **a** Shutting in the x-shuttle. **b** Shutting in the x-shuttle up to QD X_{17} followed by y-shuttle.

following the looped shuttle path indicated in Fig. 3b (inset) before returning to QD X_0 , performing a readout procedure identical to the previous pulses (results noted in Fig. 3b, full pulse shown in Extended Data Fig. 3).

During each loop, the nominally empty shuttle lane which the electron is expected to have left due to the applied junction transfer atomic pulse (λ_{JR}^1 or λ_{JL}^{-1}) is operated for 25 periods (λ_x^{25} or λ_y^{-25}). This large number of additional shuttle pulses provides us high confidence that the electron is shuttled away from the center of the T-junction if the junction transfer atomic pulse fails. Thus, the detection of a failed λ_{JR}^1 or λ_{JL}^{-1} atomic pulse is ensured. As n_{loops} increases, the ratio of electron loading events and readouts (i.e. SPAM) against the number of shuttle atomic pulses decreases, rendering the resulting fidelity more sensitive to shuttle errors occurring during looping within the T-junction. This strategy allows us to measure the shuttle fidelity of looping within T-junction with extremely high accuracy.

The fidelity per charge loop F_1 (see methods) does not significantly drop below 100 % for junction transfer drive amplitudes $A_J \geq 133$ mV. The charge loops are repeated for select A_J at $v_J = 270$ mm s $^{-1}$ as a function of n_{loops} and we fit $F_{\text{total}}(n_{\text{loops}}) = F_1^{n_{\text{loops}}}$ to the resulting data (Fig. 3c, fits indicated as solid lines). The data follow these fits well, indicating statistical independence of failure of junction transfer per loop. As a sanity check, we calculate $F_{\text{total}}(A_J, n_{\text{loops}} = 10,000)$ from the determined $F_1(A_J)$ (crosses in Fig. 3b), which agrees with the directly measured results (dots in Fig. 3b) at $v_J =$

270 mm s $^{-1}$.

To further resolve the transfer fidelity, the experiment is repeated at $A_J = 260$ mV for large n_{loops} with complete results noted in Table 1. We additionally reduce the junction transfer drive amplitude to its approximate reliable minimum $A_J = 100$ mV, which at $n_{\text{loops}} = 10^6$ and $v_J = 270$ mm s $^{-1}$ yields $F_1 = 100.0000000^{+0}_{-9 \times 10^{-7}} \%$, not significantly differing from the result at $A_J = 260$ mV.

We can feed the applied pulses back to the simulation to investigate the expected quantum states during shuttling with $A_J = 260$ mV and $A_J = 100$ mV (Supplementary Note I). The simulation indicates that the electron is continuously moved around the T-junction.

MULTIPLE ELECTRON OPERATION

Next, we verify whether arbitrary, periodic electron patterns – the filling (empty or singly occupied) of multiple QDs in the device [21] – can be simultaneously prepared in both the x- and the y-shuttle. We start by loading different electron patterns into the right half of the x-shuttle, followed by shuttling the pattern via repeated $\lambda_{JR}^1 \lambda_x^{-1} \lambda_y^{-1}$ -pulses into the y-shuttle and loading a new pattern into the entire x-shuttle, all with $A_x = A_y = A_J = 260$ mV and $v_\lambda = v_J = 270$ mm s $^{-1}$. Finally, we read-out both shuttle lanes in reverse order (Fig. 4a, exemplary pulse in Extended Data Fig. 5c). Note that in particular for patterns with high QD occupancy, e.g. $\overline{1}$, it is impossible to differentiate unin-

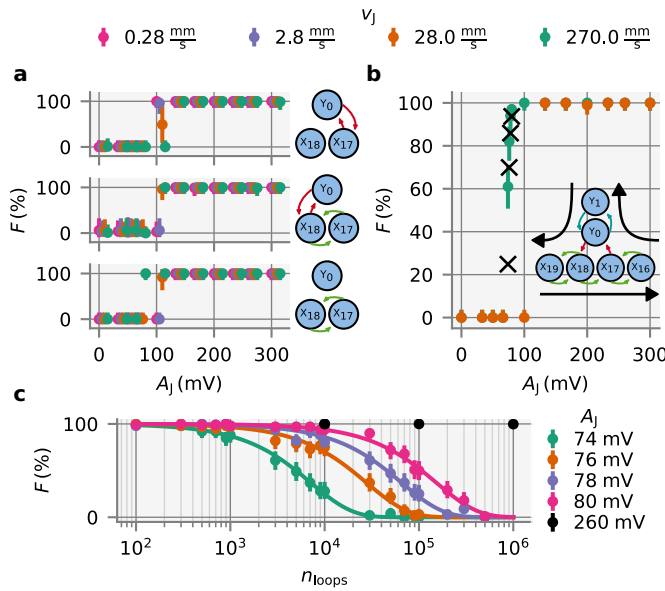


Fig. 3. Parameter variation and charge looping within the T-junction. $n_{\text{total}} = 100$, $A_x = A_y = 260$ mV and $v_\lambda = 270$ mm s $^{-1}$ for all measurements if not otherwise indicated. **a** Pulse fidelity at different drive amplitudes A_J and shuttle velocities v_J during shuttling in the junction. Additional shuttling into the y-shuttle is not shown schematically. Data points offset in A_J by 5 mV per v_J value starting from $v_J = 0.28$ mm s $^{-1}$. Error bars are $4\sigma_{F_{\text{total}}}^{\pm}$. **b** Fidelity at different drive amplitudes A_J and shuttle velocities v_J during looped inter-lane junction transfer for $n_{\text{loops}} = 10,000$. Black crosses are interpolated from F_1 extracted in (c). Error bars are $1\sigma_{F_{\text{total}}}^{\pm}$. **c** Pulse fidelity for different numbers of loops n_{loops} at $v_J = 270$ mm s $^{-1}$ and select drive amplitudes A_J for the same pulse as (b). $n_{\text{total}} = 1000$ and $n_{\text{total}} = 490$ for $A_J = 260$ mV at $n_{\text{loops}} = 10^5$ and $n_{\text{loops}} = 10^6$, respectively. Error bars are $1\sigma_{F_{\text{total}}}^{\pm}$.

tentional electron tunneling from a SPAM error during L_1 resulting in the detection of two electrons in the same QD. Therefore, we eliminate all pulses with two electrons detected in any QD from the QD occupancy counts. In the calculation of F_{total} , we count a pulse as successful (failed) if one or two electrons are detected in a QD with one electron (zero electrons) expected (see methods).

Remarkably, simultaneous shuttling and routing of up to 54 electrons in the two independent shuttle lanes yields fidelities of $F_{\text{total}} \approx 99\%$. The main error is detection of additional electrons (red in Fig. 4b) due to unintentional loading of electrons (i.e. SPAM errors) caused by uncompensated drift in the L_0 atomic pulse. Importantly, tunneling across neighboring QDs is not observed except from QD Y_{17} (red/blue in Fig. 4b), presumably due to the large potential barrier at the edge of the y-shuttle.

An interesting feature of the T-junction is the ability to perform a native spin-SWAP gate by swapping electron positions. This can replace the exchange-based spin-SWAP gate, the fidelity of which is low due to need of diabatic switching of the exchange interaction [32]. Here,

the SWAP operation is emulated without spin control by swapping the electron order of two consecutively prepared electron patterns utilizing the independent control of the x- and y-shuttle (Fig. 4c with the pulse shown in Extended Data Fig. 5d). We observe pulse fidelities $F_{\text{total}} \geq 99.8\%$ (Fig. 4d), independent of the initial order of the two prepared patterns.

CONCLUSIONS

We demonstrate single electron routing across a conveyor-mode shuttling based T-junction in Si/SiGe. In general, the charge shuttle fidelity is high with particularly high charge transfer fidelity of $F = 100.0000000^{+0}_{-9} \times 10^{-7}\%$ in the center of the T-junction. This is remarkable as most gates of the T-junction are connected and no tuning of voltages applied to individual gates is performed. Such fine-tuning is common for state-of-the-art qubit devices, posing a challenge for device scalability. We operate the T-junction device that consists of 54 QDs by only eleven voltage channels, three of which required solely for charge initialization and readout by a single-electron transistor (SET). In total, we need only 5 DC voltages including one voltage to form the barriers for the top and left end of the shuttle lanes and 4 voltages to form the SET. Eight short atomic voltage pulses, from which we easily compile complex pulses by an arbitrary waveform generator, are sufficient to operate the whole T-junction device. These pulses can control up to 54 electrons with arbitrary single electron fillings of all QDs with high accuracy. In particular, we use our T-junction to swap electron positions with fidelity exceeding the fidelity of an exchange-based SWAP gate commonly used for spin qubits.

Controlling positions of many single electrons with simple voltage pulses in two dimensions has important implications especially addressing the scalability of spin-based quantum computation. The voltage tuning is simple and fast and fewer signal generators are needed. In fact, our T-junction has been operated in two thermal cycles without need of voltage fine-tuning. Such high level of control can be exploited for novel low-power classical electronics operating with single electrons in QDs below 1 K. It is also promising for fault-tolerant quantum computing with spin qubits, for which millions of electrons have to be positioned in a two-dimensional matrix of shuttle lanes. In such lanes, spin-qubit shuttling with high velocity and spin manipulation has been demonstrated. Ultimately, in a sufficiently sparse two-dimensional qubit architecture, classical control electronics could be co-integrated on the quantum chip [27].

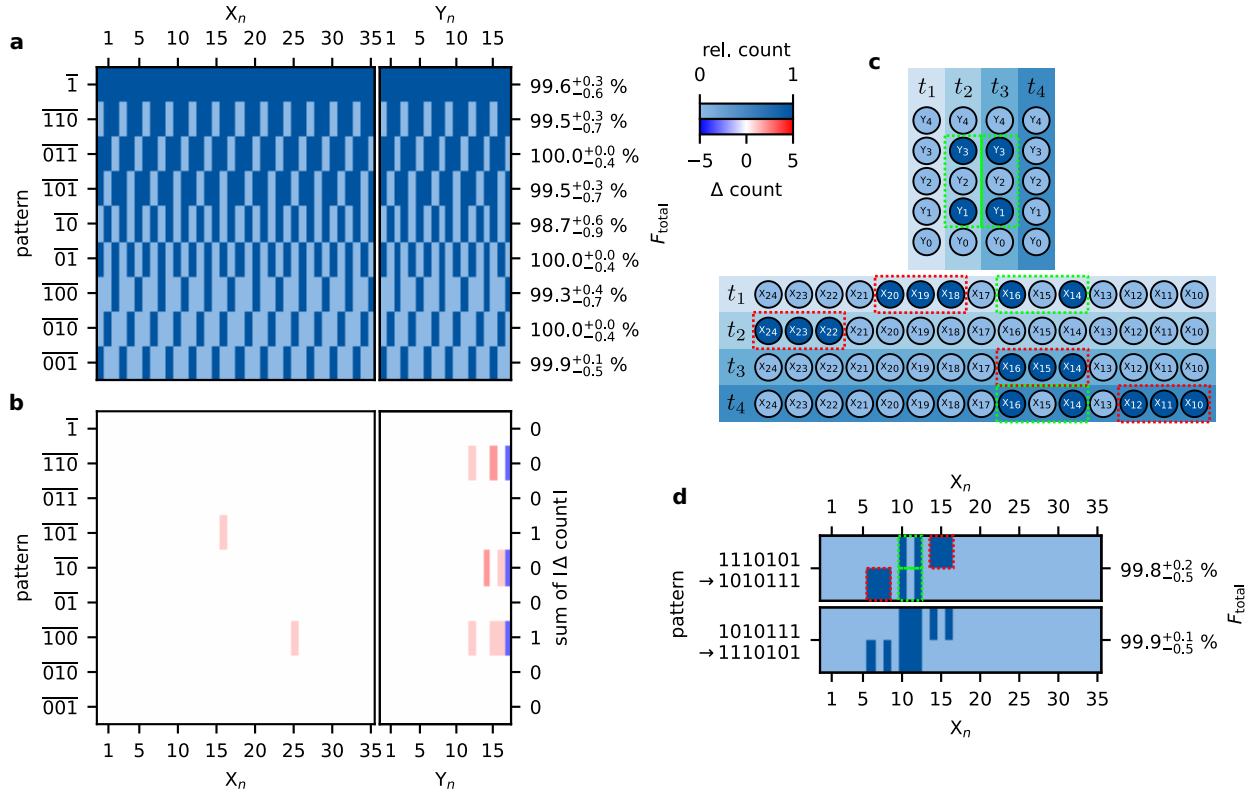


Fig. 4. Multiple electron operation. Color bars apply to (a), (b) and (d). Blue color bar: average QD occupancy over pulse repetitions. Blue-red color bar: Sum of QD occupancy deviating from expectation over pulse repetitions. $n_{\text{total}} = 1000$ for each electron pattern and SWAP. If two electrons are detected in the same QD, the total result of the pulse is excluded from occupancy counts while remaining included in the calculation of F_{total} . **a** Results for loading periodic electron occupancy patterns into the x- and y-shuttle. The patterns are held in both channels simultaneously. Overline notation to the left of the plot identifies the periodic patterns. The total fidelity of each pattern is displayed to the right. **b** Deviation from expectation in (a). Sum of absolute sum of deviations over all repetition over all repetitions is noted to the right. **c** Expected charge configuration of a section of the x- and y-shuttle when performing an electron pattern SWAP. Dark blue QD: one electron in QD. Light blue QD: no electron in QD. The leading and following patterns are outlined in red and green, respectively. Labels t_1 through t_4 indicate four time steps during the pulse. t_1 : The two sequential patterns are shuttled to the junction. t_2 : The following pattern is transferred into the y-shuttle. t_3 : The leading pattern is retracted. t_4 : The following pattern is retrieved and the pattern SWAP is complete. **d** Results for pattern SWAP. Patterns are highlighted matching (c). Pulse fidelities are shown to the right. The deviation from expectation is noted in Extended Data Fig. 4.

- [1] Burkard, G., Ladd, T. D., Pan, A., Nichol, J. M. & Petta, J. R. Semiconductor spin qubits. *Rev. Mod. Phys.* **95**, 025003 (2023).
- [2] Noiri, A. *et al.* Fast universal quantum gate above the fault-tolerance threshold in silicon. *Nature* **601**, 338–342 (2022).
- [3] Unseld, F. K. *et al.* Baseband control of single-electron silicon spin qubits in two dimensions. *Nat. Commun.* **16**, 5605 (2025).
- [4] Mills, A. R. *et al.* Two-qubit silicon quantum processor with operation fidelity exceeding 99 %. *Sci. Adv.* **8** (2022).
- [5] Xue, X. *et al.* Quantum logic with spin qubits crossing the surface code threshold. *Nature* **601**, 343–347 (2022).
- [6] George, H. C. *et al.* 12-Spin-Qubit Arrays Fabricated on a 300 mm Semiconductor Manufacturing Line. *Nano Lett.* **25**, 793–799 (2025).
- [7] Philips, S. G. J. *et al.* Universal control of a six-qubit quantum processor in silicon. *Nature* **609**, 919–924 (2022).
- [8] Weinstein, A. J. *et al.* Universal logic with encoded spin qubits in silicon. *Nature* **615**, 817–822 (2023).
- [9] Zhang, X. *et al.* Universal control of four singlet–triplet qubits. *Nat. Nanotechnol.* **20**, 209–215 (2025).
- [10] Hendrickx, N. W. *et al.* Sweet-spot operation of a germanium hole spin qubit with highly anisotropic noise sensitivity. *Nat. Mater.* **23**, 920–927 (2024).
- [11] John, V. *et al.* Robust and localised control of a 10-spin qubit array in germanium. *Nat. Commun.* **16**, 10560 (2025).
- [12] Vandersypen, L. M. K. *et al.* Interfacing spin qubits in quantum dots and donors — hot, dense, and coherent. *npj Quantum Inf.* **3**, 34 (2017).
- [13] Boter, J. M. *et al.* Spiderweb Array: A Sparse Spin-Qubit

Array. *Phys. Rev. Appl.* **18**, 024053 (2022).

[14] Taylor, J. M. *et al.* Fault-tolerant architecture for quantum computation using electrically controlled semiconductor spins. *Nat. Phys.* **1**, 177–183 (2005).

[15] Ginzel, F. *et al.* Scalable parity architecture with a shuttling-based spin qubit processor. *Phys. Rev. B* **110**, 075302 (2024).

[16] Fujita, T., Baart, T. A., Reichl, C., Wegscheider, W. & Vandersypen, L. M. K. Coherent shuttle of electron-spin states. *npj Quantum Inf.* **3**, 22 (2017).

[17] Zwerver, A. *et al.* Shutting an Electron Spin through a Silicon Quantum Dot Array. *PRX Quantum* **4**, 030303 (2023).

[18] Foster, N. D., Henshaw, J. D., Rudolph, M., Luhman, D. R. & Jock, R. M. Dephasing and error dynamics affecting a singlet-triplet qubit during coherent spin shuttling. *npj Quantum Inf.* **11**, 63 (2025).

[19] De Smet, M. *et al.* High-fidelity single-spin shuttling in silicon. *Nat. Nanotechnol.* **20**, 866–872 (2025).

[20] Seidler, I. *et al.* Conveyor-mode single-electron shuttling in Si/SiGe for a scalable quantum computing architecture. *npj Quantum Inf.* **8**, 100 (2022).

[21] Xue, R. *et al.* Si/SiGe QuBus for single electron information-processing devices with memory and micron-scale connectivity function. *Nat. Commun.* **15**, 2296 (2024).

[22] Struck, T. *et al.* Spin-EPR-pair separation by conveyor-mode single electron shuttling in Si/SiGe. *Nat. Commun.* **15**, 1325 (2024).

[23] Volmer, M. *et al.* Mapping of valley splitting by conveyor-mode spin-coherent electron shuttling. *npj Quantum Inf.* **10**, 61 (2024).

[24] Volmer, M. *et al.* Reduction of the impact of the local valley splitting on the coherence of conveyor-belt spin shuttling in $^{28}\text{Si}/\text{SiGe}$. Preprint at <https://arxiv.org/abs/2510.03773> (2025).

[25] Langheinrich, W. *et al.* Fabrication of single-electron shuttling channels in a silicon CMOS fab using high-throughput electron beam lithography. *40th European Mask and Lithography Conference (EMLC 2025)*, Proc. SPIE 13787, 137870K (SPIE, 2025).

[26] Langrock, V. *et al.* Blueprint of a scalable spin qubit shuttle device for coherent mid-range qubit transfer in disordered Si/SiGe/SiO₂. *PRX Quantum* **4**, 020305 (2023).

[27] Künne, M. *et al.* The SpinBus architecture for scaling spin qubits with electron shuttling. *Nat. Commun.* **15**, 4977 (2024).

[28] David, A. *et al.* Long distance spin shuttling enabled by few-parameter velocity optimization Preprint at <https://arxiv.org/abs/2409.07600> (2024).

[29] Jain, S. *et al.* Penning micro-trap for quantum computing. *Nature* **627**, 510–514 (2024).

[30] Barredo, D., de Léséleuc, S., Lienhard, V., Lahaye, T. & Browaeys, A. An atom-by-atom assembler of defect-free arbitrary two-dimensional atomic arrays. *Science* **354**, 1021–1023 (2016).

[31] Delaney, R. D. *et al.* Scalable Multispecies Ion Transport in a Grid-Based Surface-Electrode Trap. *Phys. Rev. X* **14**, 041028 (2024).

[32] Nowack, K. C. *et al.* Single-Shot Correlations and Two-Qubit Gate of Solid-State Spins. *Science* **333**, 1269–1272 (2011).

[33] Klos, J., Hassler, F., Cerfontaine, P., Bluhm, H. & Schreiber, L. R. Calculation of tunnel couplings in open gate-defined disordered quantum dot systems. *Phys. Rev. B* **98**, 155320 (2018).

[34] Albrecht, W., Moers, J. & Hermanns, B. HNF - Helmholtz Nano Facility. *JLSRF* **3**, A112 (2017).

METHODS

Device fabrication

The device is fabricated on an undoped $\text{Si}_{0.70}\text{Ge}_{0.30}/\text{Si}/\text{Si}_{0.70}\text{Ge}_{0.30}$ heterostructure, which is grown on multiple buffer layers on a (001) CVD-grown silicon wafer. All silicon in this experiment is of natural isotope composition. The tensile strained, nominally 10 nm thick Si layer forms a quantum well hosting a two-dimensional electron gas. The upper $\text{Si}_{0.70}\text{Ge}_{0.30}$ layer has a nominal thickness of 30 nm and is capped with 2 nm of Si. The lower $\text{Si}_{0.70}\text{Ge}_{0.30}$ layer has a nominal thickness of 2 μm with an intermediate, chemically-mechanically polished step after 1 μm . Beneath the buffer, a nominally 3 μm thick linearly graded $\text{Si}_{1-x}\text{Ge}_x$ ($x \in [0.05, 0.3]$) buffer is deposited on the substrate silicon wafer.

Ohmic contacts are fabricated by phosphorus ion implantation and thermal activation at 730 °C for 30 s. The three metal gate layers are made of a Ti/Pt stack (5 nm and 15 nm/22 nm/29 nm, respectively), shaped by 100 keV electron-beam lithography (schematics of gate layers in Extended Data Fig. 6.) and lift-off, isolated from each other and the substrate by amorphous, 10 nm thick layers of Al_2O_3 , fabricated by atomic layer deposition.

Device design and operation

The lowest gate layer is comprised of three large, grounded screening gates (ScrTL, ScrTR, ScrBR) transversely confining two $\approx 5 \mu\text{m}$ and $\approx 10 \mu\text{m}$ long one-dimensional electron channels (1DECs) joining at a 90° angle in the device center, while confinement into quantum dots along the channels is achieved via 4 claviature gates per channel in gate layers two (LS2, RS2, TS2, LS4, RS4 and TS4) and three (LS1, RS1, TS1, LS3, RS3 and TS3). Six individual gates (JLS, JLP, JP, JRP, JRS and JTS) could enable independent control in the critical junction center. The electron channels are terminated towards the edges of the device with three individual gates each (TLB1/2, TLP, TRB1/2, TRP, TTB1/2 and TTP), beyond which a single electron transistor (SET) each is formed. The right SET serves as an electron reservoir and proximal charge detector [33]. In total 218 claviature gates span the 1DECs, forming the two shuttle lanes.

Due to the periodic gating defining the shuttle lanes, several gates in each lane are grouped into gate sets, following the color coding in Fig. 1. To all gates within one gate set, the same voltage is applied. The eight periodic gate sets are: $S_{x,1} = \text{TLB1/2, TLP, LS3, JRP and RS1}$; $S_{x,2} = \text{TLB2, LS4, JLS, JRS, TRB2 and RS4}$; $S_{x,3} = \text{LS1, JLP and RS3}$; $S_{x,4} = \text{LS2, JP and RS2}$; $S_{y,1} = \text{TTP and TS3}$; $S_{y,2} = \text{TTB2 and TS4}$; $S_{y,3} = \text{TS1}$; $S_{y,4} = \text{TS2 and JTS}$. Gates belonging to these gate sets, as well as TRB1, TRP and RB1 are controlled by voltage pulses.

A constant and identical DC voltage of 330 mV is applied to all gates belonging to gate sets $S_{j,i}$ ($i \in \{1, 2, 3, 4\}$, $j \in \{x, y\}$). TLB1 and TTB1 are grounded during the measurements presented in this work. TRP, TRB1 and the gates defining the right SET are tuned to individual DC voltages to facilitate charge initialization and readout.

A pulse P is defined as the set of time-dependent voltage sequences simultaneously applied as $\Delta V_g(t)$ individually specified for one or more gates g . P is applied to g in addition to the constant DC voltage specific to g . The voltage applied to gates not specified in the definition of P remains constant during the duration of the pulse. The time reverse and n consecutive repetitions of P are denoted as P^{-1} and P^n , respectively. Pulses can be composed of other pulses by applying these immediately after each other.

We define the idle state of the device such that a QD is formed under every fourth gate, $\lambda = 280 \text{ nm}$ in each shuttle lane by applying a suitable periodic confinement potential. In this idle configuration, the QD minima in the x-shuttle are centered under the $S_{x,1}$ gate set and in the y-shuttle under the $S_{y,1}$ gate set (Fig. 1f). Additionally, in order to place QD X_0 in closer proximity to the SET at the right end of the x-shuttle for readout, the readout state is defined, placing the QD minima in the x-shuttle under TRP and the $S_{x,3}$ gate set. If not otherwise stated, atomic pulses start at and return to the idle state. We label the QDs by their nominal position as indicated in Fig. 1f. While conveyor-mode shuttling continuously moves the QDs, we reassign the QD labels after each atomic pulse to match the initial QD positions. A simulation of the electron wavefunction when confined in the QDs is shown in Fig. 1g (more details in Supplementary Note I).

Starting and ending in the readout state, the charge initialization atomic pulses (Fig. 1b) are calibrated from charge stability measurements to initialize the charge occupancy of QD X_0 to either one electron (L_1) or zero (L_0), by transferring electrons between QD X_0 and a reservoir formed at the SET at the right end of the x-shuttle, similar to Ref. [21]. The charge occupancy of QD X_0 in the readout state is determined from the current across the right SET, which is tuned to its optimal sensitivity by applying the atomic pulse R_{CC} . To reset the QD occupancy for future readout, R_{CC} is always followed by unloading QD X_0 , defining the destructive readout pulse R .

From λ_x , $\lambda_{L \rightarrow R}$ and $\lambda_{R \rightarrow L} = \lambda_{L \rightarrow R}^{-1}$ are derived to transition between the idle and readout state (fig. 1c).

All finally composed pulses are either led or followed by a ROI pulse (Fig. 1e), used to recalibrate the SET current levels during the readout process. During each readout (i.e. application of R_{CC}), the current through the SET is monitored and averaged in the time interval t_{RO} . Due to the capacitive coupling of the charge present in QD X_0 in the readout state, the chemical potential of the SET's sensing is altered, leading to proximal charge

detection by the current across the SET.

We can use the resulting current to readout the number of electrons occupying QD X_0 using the following procedure: First, the current background as well as current thresholds allowing determination of the number of electrons in QD X_0 are extracted. The background and thresholds are calculated block-wise over differing numbers of repetitions to accommodate changing system noise and SET current drift. The background in one pulse repetition is calculated by averaging the measured current during all readouts in each pulse repetition and then averaged over the current block of repetitions. The background is subtracted from the measured current. The reference readouts directly following the L_1 and L_0 atomic pulses within the ROI pulse contained in each pulse repetition are used to determine the current thresholds discriminating the number of electrons in QD X_0 . To make the observed threshold robust against unintentionally incorrect charge occupancy of QD X_0 , we remove the 5 % largest and smallest readout currents each from the calculation. The threshold discriminating between zero and one electrons is set as the mid-point between the average current in the reference readouts and then averaged over the current block of repetitions.

It becomes apparent that in $\approx 0.04\%$ of readouts, two electrons are unexpectedly detected in QD X_0 . While a clear distinction between outliers in the current during the detection of one electron and the detection of two electrons can not always be made, we still attempt to make this discrimination. The corresponding threshold discriminating between one and two electrons detected is set $4 \cdot \sigma_{L_1}$ beyond the average current during the reference readout after L_1 , where σ_{L_1} is the population standard deviation of the average measured currents during this readout, taken over the current block of repetitions.

To clear the otherwise fully depleted shuttle lanes from remaining charges of previous experiments, a flush pulse, similar to Ref. [21] (Extended Data Fig. 5a), is applied at irregular intervals using $A_x = A_y = A_J = 260$ mV.

Experimental setup

The device is mounted on the mixing chamber stage of an Oxford Instruments wet dilution refrigerator at a temperature of ≈ 30 mK. Signals inside the refrigerator are carried to the sample via custom-made high density flexible flat cables with a bandwidth on the order of 1 MHz. This bandwidth allows for experimentation close to the frequency range used for spin-coherent single electron shuttling [26]. At room temperature, voltages applied to gates that are held constant are generally applied using custom-made low noise digital to analog converters. Voltages are applied to pulsed gates using Zürich Instruments HDAWG arbitrary waveform generators. The two ohmic contacts of the SET used for readout are connected to room-temperature bias-tees allowing for an offset voltage as well as a modulated voltage to be applied and a

modulated current to be measured. For the results presented here, the offset voltage is set to 0 V while the modulated voltage on the order of 100 μ V is applied using the output of a Zürich Instruments MFLI lock-in amplifier. The modulated current is then converted to a voltage by a Basel Precision Instruments transimpedance amplifier which is measured using the lock-in amplifier. For ease of integration, the demodulated signal is converted to an appropriately scaled voltage output by the lock-in amplifier, buffered by a Stanford Research Systems SR560 preamplifier and acquired using an AlazarTech ATS9440 waveform digitizer.

Fidelity calculation and error estimation

We consider the result of a shuttle pulse containing several atomic readout pulses a success, if electrons are detected during and only during the readout pulses for which we expect electrons to be detected. Thus, a pulse in which an electron is detected where no electron is expected is considered a failed pulse. If n_s is the number of successful pulse repetitions and n_{total} is the total number of repetitions, the pulse fidelity F_{total} is defined as:

$$F_{\text{total}} = \frac{n_s}{n_{\text{total}}}.$$

The generally asymmetric uncertainty on F_{total} is determined from the two-sided, 95 % Clopper-Pearson confidence interval $[F_{\text{total}, 95\%}^-, F_{\text{total}, 95\%}^+]$ as $\sigma_{F_{\text{total}}}^{\pm} = F_{\text{total}, 95\%}^{\pm} - F_{\text{total}}$. The value of F_{total} and its uncertainty is denoted as $(F_{\text{total}})_{\sigma_{F_{\text{total}}}^{\pm}}$.

Occasionally, we observe from the SET current level that two electrons instead of one expected electron are detected. For these rare cases, we still label the repetition as successful, as we attribute the observation to the unintended loading of an additional electron presumably during the intended electron loading, which constitutes a SPAM error. The detection of an additional electron in the QD, in which one electron is expected due to the application of L_1 , is explained by the conveyor-mode shuttle operating with doubly occupied QDs. While the determination of this observation as a success reduces the impact of SPAM errors on the pulse fidelity, it is stricter on the fidelity of charge shuttling, as the confinement of two electrons in a QD is expected to be weaker and therefore more prone to shuttle errors than shuttling only one electron, e.g. one electron tunneling into a neighboring, unoccupied QD.

Fidelity calculation for looping in the T-junction

The fidelity per charge loop F_1 and the corresponding uncertainties $\sigma_{F_1}^\pm$ are calculated following:

$$F_1 = F_{\text{total}}^{\frac{1}{n_{\text{loops}}}}$$

$$\sigma_{F_1}^\pm = (F_{\text{total}, 95\%}^{\pm})^{\frac{1}{n_{\text{loops}}}} - F_1$$

These values are denoted as $(F_1)_{\sigma_{F_1}^\pm}^{\pm}$.

DATA AVAILABILITY

The data generated in this study are available in the Zenodo repository under <https://doi.org/10.5281/zenodo.18032292>.

ACKNOWLEDGEMENTS

We acknowledge the support of the Dresden High Magnetic Field Laboratory (HLD) at the Helmholtz-Zentrum Dresden - Rossendorf (HZDR), member of the European Magnetic Field Laboratory (EMFL). This work was funded by the German Research Foundation (DFG) within the project 421769186 (SCHR 1404/5-2) and under Germany's Excellence Strategy - Cluster of Excellence Matter and Light for Quantum Computing (ML4Q) EXC 2004/2 - 390534769, and by the European Union's Horizon Research and Innovation Actions under Grant Agreement No. 101174557 (QLSI2). The device fabrication has been done at HNF - Helmholtz Nano Facility, Research Center Juelich GmbH [34].

AUTHOR CONTRIBUTIONS STATEMENT

M.B. carried out the experiments and simulation presented in this work. M.B. analyzed the data with L.R.S. Sample screening and pre-characterization was carried out by L.D. guided by M.B.. Custom components and the control electronic scheme were designed by M.B.. M.B. adapted the device fabrication process developed by R.X., J.S.T., and I.S. and carried out the fabrication. Electron beam lithography was carried out by S.T.. M.B. and P.S. operated the dilution refrigerator. L.R.S. and M.B. designed the device and L.R.S. supervised the study. L.R.S. and H.B. provided guidance to all authors. M.B. and L.R.S wrote the manuscript, which was commented by all other authors.

COMPETING INTERESTS

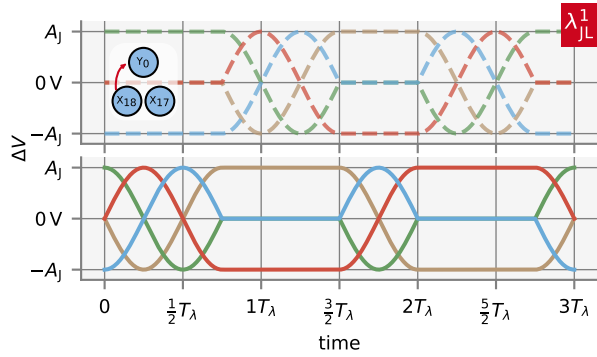
H.B, L.R.S., R.X., I.S. are co-inventors of patent applications that cover conveyor-mode shuttling and/or its

applications. L.R.S. and H.B. are founders and shareholders of ARQUE Systems GmbH. The other authors declare no competing interest.

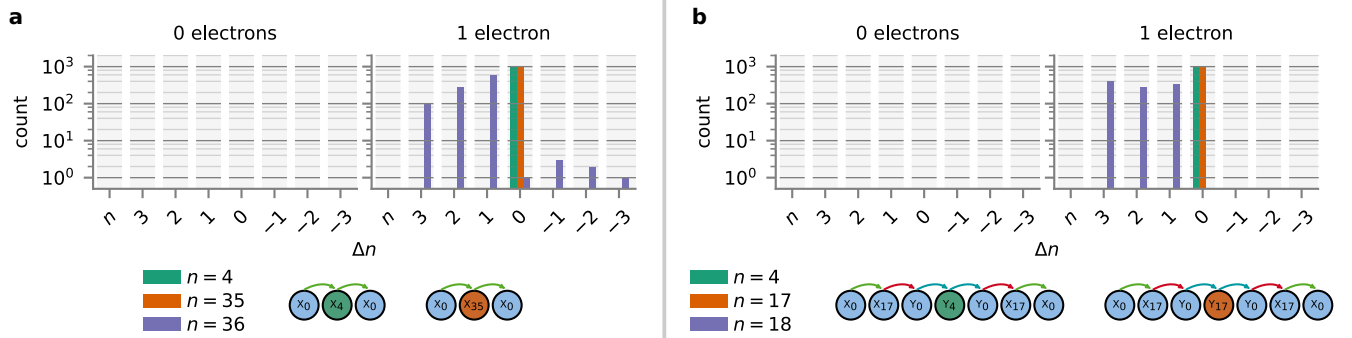
Table 1. Shuttle fidelities at $A_x = A_y = A_J = 260\text{ mV}$ and $v_\lambda = v_J = 270\text{ mm s}^{-1}$. Shuttle paths are indicated as sequences of key QDs traversed in time-order. $X_0 (X_{16} Y_1 X_{19})^{10^6} X_0$ with $A_J = 100\text{ mV}$ yields $F_1 = 100.0000000_{-9 \times 10^{-7}}^{+0}\%$.

shuttle path	$F_{\text{total}} (\%)$	$F_1 (\%)$
$X_0 X_4 X_0$	$99.9_{-0.5}^{+0.1}$	
$X_0 X_{35} X_0$	$100.0_{-0.4}^{+0.0}$	
$X_0 X_{17} Y_0 Y_4 Y_0 X_{17} X_0$	$100.0_{-0.4}^{+0.0}$	
$X_0 X_{17} Y_0 Y_{17} Y_0 X_{17} X_0$	$100.0_{-0.4}^{+0.0}$	
$X_0 (X_{16} Y_1 X_{19})^{10^5} X_0$	$100.0_{-0.4}^{+0.0}$	$100.00000000_{-4 \times 10^{-6}}^{+0}$
$X_0 (X_{16} Y_1 X_{19})^{10^6} X_0$	$99.8_{-0.9}^{+0.2}$	$99.999998_{-9 \times 10^{-7}}^{+2 \times 10^{-7}}$

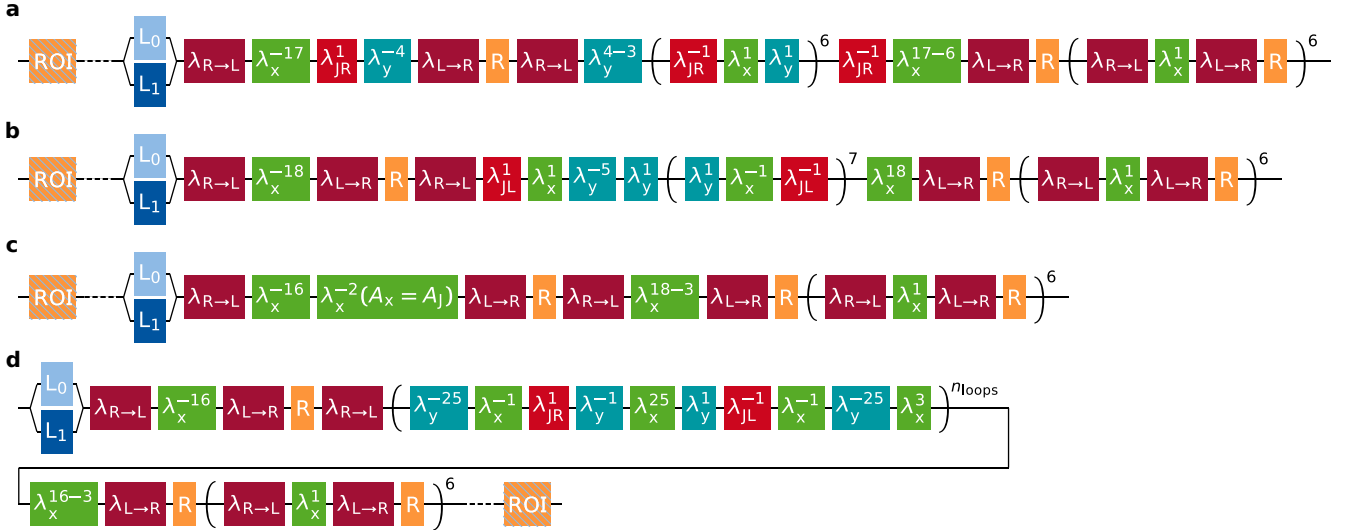
EXTENDED DATA



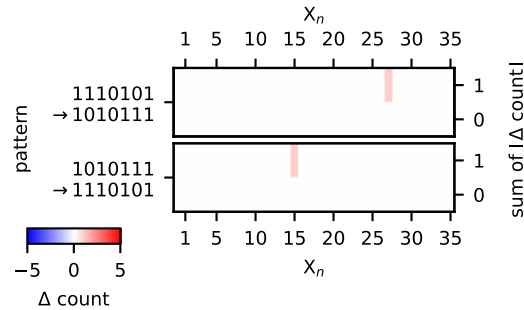
Extended Data Fig. 1. **Junction transfer atomic pulse λ_{JL}^1** This figure follows the legend in Fig. 1. The atomic pulse shown shuttles the charge in QD X_{18} to QD Y_0 .



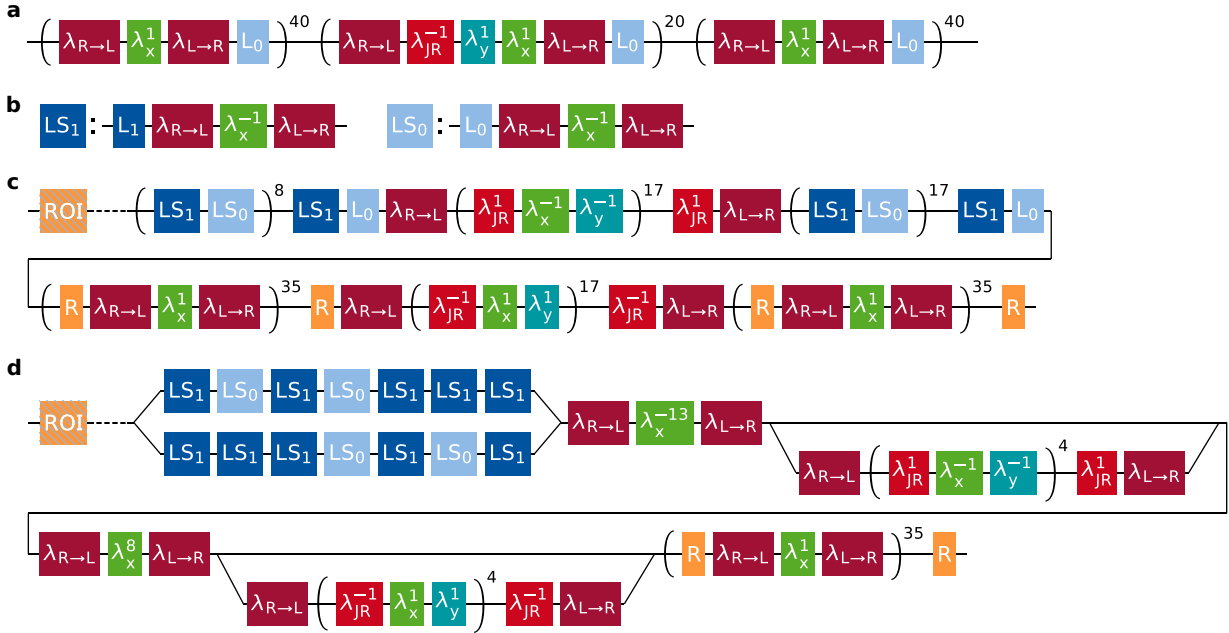
Extended Data Fig. 2. **Verifying shuttling in the x- and y-shuttles.** Complementary results of Fig. 2 at $v_\lambda = v_J = 28 \text{ mm s}^{-1}$. **a** Shutting in the x-shuttle. **b** Shutting in the x-shuttle up to QD X_{17} followed by the y-shuttle.



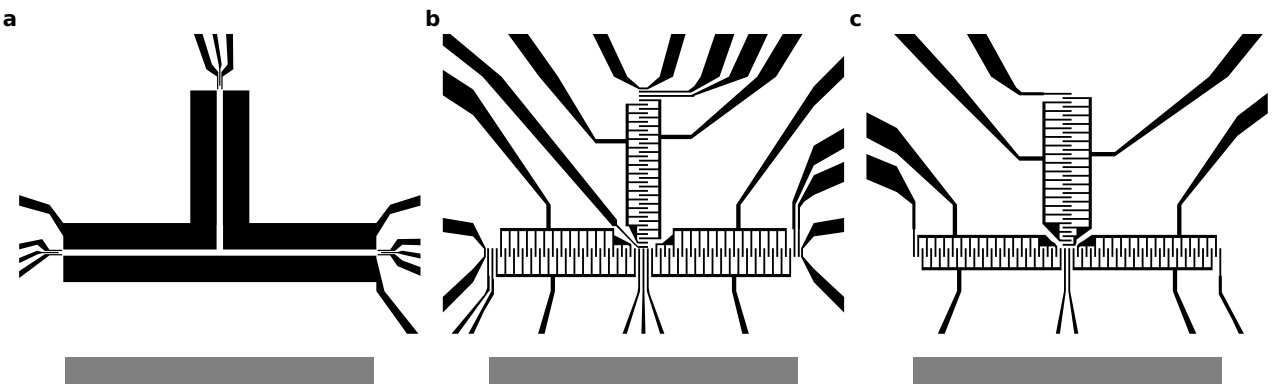
Extended Data Fig. 3. **Pulses applied to explore parameter space of junction shuttling.** **a-c** Pulses used for results in Fig. 3a. **d** Pulse used for results in Fig. 3b and Fig. 3c. Note that pairs of $\lambda_{L \rightarrow R} \lambda_{R \rightarrow L}$ and their reverse are removed by a simplification step before playback.



Extended Data Fig. 4. **Error counts for pattern SWAP.** Complementary data for Fig. 4d following the same color map.



Extended Data Fig. 5. **Additional pulses.** **a** Flush pulse. Due to the extensive use of slow L_0 pulses, the flush is not performed before every pulse repetition. During the flush $A_J = 260$ mV and the same shuttle velocities used during the rest of the pulse are applied. **b** Load and shuttle notation shorthand. **c** Exemplary pulse for shuttle of 10-electron pattern. For other electron patterns, only the initialization pulses are modified accordingly. **d** Pulse applied in Fig. 4c and Fig. 4d to perform SWAP of an electron pattern. The top and bottom initialization branches (first row) as well as the top and bottom shuttling branches (second row) are combined to yield 4 different pulses. The bottom shuttling branch performs the SWAP. Note that pairs of $\lambda_{L\rightarrow R}\lambda_{R\rightarrow L}$ and their reverse are removed by a simplification step before playback.



Extended Data Fig. 6. **Metal gate layers defining the device.** Dark shapes correspond to metalized regions visible in Fig. 1a. Scale bars are 10 μm . **a** First metal layer. **b** Second metal layer. **c** Third metal layer.

SUPPLEMENTARY INFORMATION

Supplementary Note I: Simulation of shuttling in the T-junction

We simulate the wavefunction of an electron confined to a quantum dot (QD) in the device by solving the one-electron time independent Schrödinger equation on a two-dimensional grid on the gate-controlled instantaneous potential landscape at many time steps within a suitable region around the expected electron position. The total potential within the Si/SiGe quantum well for each time step is calculated in COMSOL Multiphysics® using a model of the device. During the calculation we disregard charge screening within the quantum well as the relevant device region is expected to be almost fully depleted. To verify continuous electron motion, we evaluate the expectation value of the ground state position $\langle x_i \rangle = \langle g | x_i | g \rangle$, where $x_i \in \{x, y\}$ is the x- or y-coordinate, and $|g\rangle$ is the electron ground state. Analogous to Ref. [1], we also calculate the resulting orbital splitting $E_{\text{orb}} = \langle e | H | e \rangle - \langle g | H | g \rangle$ between $|g\rangle$ and the first excited state $|e\rangle$, where H is the system Hamiltonian.

As the central device aspect, we simulate shuttling from QD X_{16} to QD Y_0 using $A_x = A_y = A_J = A$, twice using $A = 260$ mV and $A = 100$ mV, respectively as well as similar DC voltages as used in the experiment. The results are shown in Supplementary Figure 1a-c and Supplementary Figure 1e-g, with probability densities for key time steps rendered in Supplementary Figure 1d and Supplementary Figure 1h. Renderings of full simulations are shown in Supplementary Video 1 ($A = 260$ mV) and Supplementary Video 2 ($A = 100$ mV).

Coinciding with the respective minimum in E_{orb} for both drive amplitudes, a fast increase in $\langle y \rangle$ is obtained. This increase is more pronounced for $A = 100$ mV compared to $A = 260$ mV, however both $\langle x \rangle$ and $\langle y \rangle$ are continuous for both drive amplitudes indicating that electron transfer occurs without long-range tunneling (Supplementary Figure 1a, e).

The minima in E_{orb} occur near $2T_\lambda$, decreasing to $E_{\text{orb},\text{min}} \approx 910$ μeV and $E_{\text{orb},\text{min}} \approx 185$ μeV for $A = 260$ mV and $A = 100$ mV, respectively. Further inspection reveals the cause for this decrease as the lowered confinement when merging the QD containing the electron and the first QD of the vertical conveyor. As E_{orb} decreases, excitation into the excited state may occur, even at low shuttle velocities. If the occupancy of these states is uncontrolled and orbital relaxation occurs slowly or excitations occur often, spin state decoherence occurs, as the electron g -factor and valley splitting are expected to differ significantly between ground and excited states [2, 3], warranting further investigation. We estimate that realistic potential disorder, caused by e.g. charged defects in the semiconductor-oxide interface above the Si capping layer, could decrease $E_{\text{orb},\text{min}}$ into a problematic regime for $A = 100$ mV (c.f. Ref. [1]).

When sufficiently far away from the junction center, a consistent primary confinement axis with respect to the shuttle direction is observed, when the electron is centered below a gate. For $A = 260$ mV, this axis is aligned longitudinally with the shuttle direction (indicating stronger confinement by shuttle gates) and for $A = 100$ mV it is aligned transversely (indicating stronger confinement by screening gates). We refer to the initial and final excited states during the simulation as $|e_x\rangle$ and $|e_y\rangle$, respectively, and plot the projection of the instantaneous first excited state onto these states in Supplementary Figure 1b and Supplementary Figure 1f.

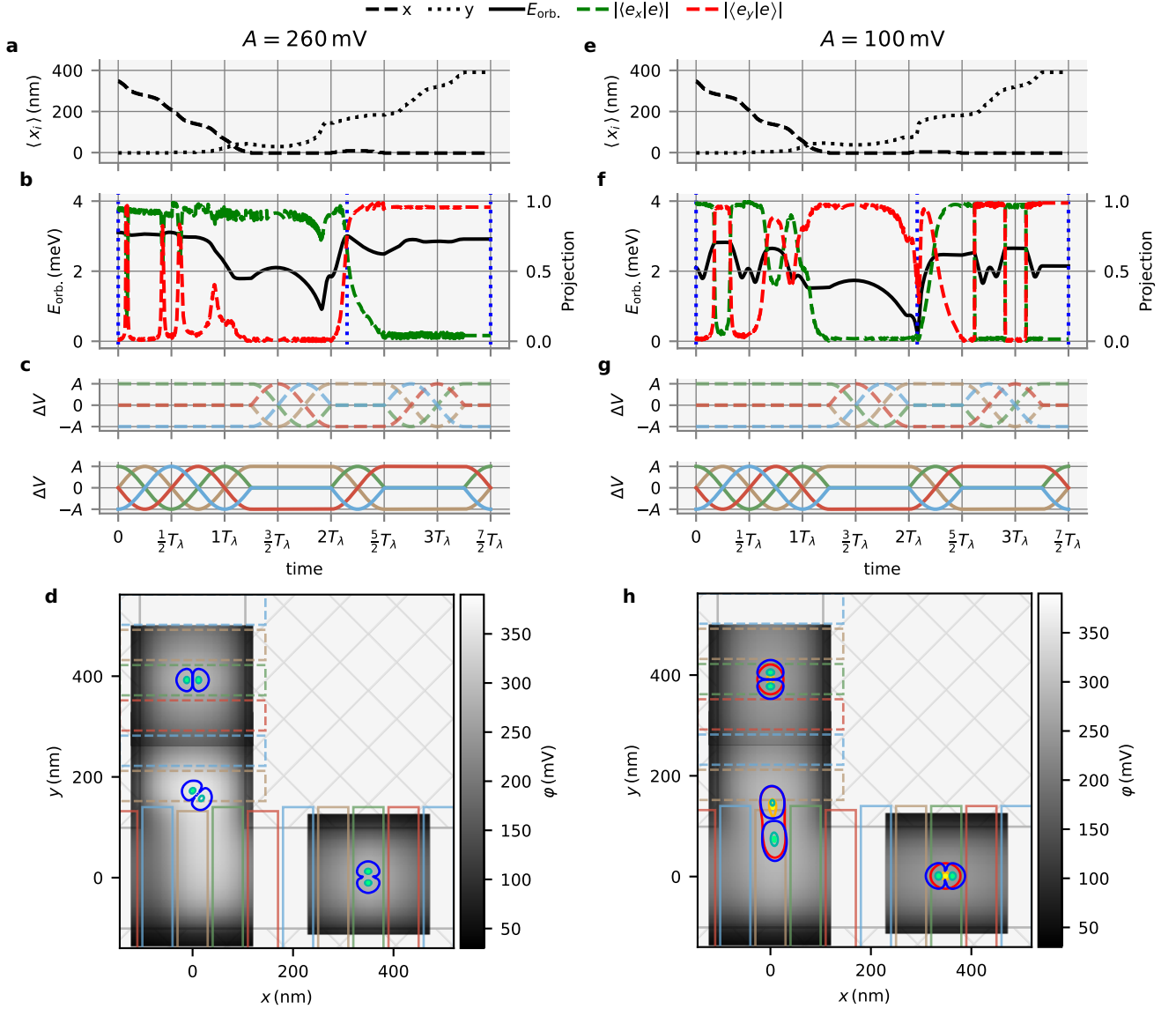
For $A = 260$ mV, the first excited states remain well aligned with the primary confinement axes, except for short lived rotations when the electron is centered between two gates. Using this metric, the moment of transfer between the x- and y-shuttle can be identified when the first excited state rotates by 90°, coinciding with a maximum in E_{orb} .

For $A = 100$ mV, this rotation still occurs during this transfer, however similar rotations occur at several time steps as the confinement strength varies with the height of the gate the electron is currently under. Tuning drive amplitude and DC voltage separately for each gate layer is expected to suppress these additional rotations. Additionally, no maximum in E_{orb} is observed in the moment of transfer due to the weak confinement in the junction center, as indicated by the low $E_{\text{orb},\text{min}}$ and the non-circular electron probability density.

[1] Langrock, V. *et al.* Blueprint of a scalable spin qubit shuttle device for coherent mid-range qubit transfer in disordered Si/SiGe/SiO₂. *PRX Quantum* **4**, 020305 (2023).

[2] Volmer, M. *et al.* Mapping of valley splitting by conveyor-mode spin-coherent electron shuttling. *npj Quantum Inf.* **10**, 61 (2024).

[3] Struck, T. *et al.* Spin-EPR-pair separation by conveyor-mode single electron shuttling in Si/SiGe. *Nat. Commun.* **15**, 1325 (2024).



Supplementary Figure 1. **Additional simulation results for $A = 260$ mV and $A = 100$ mV.** $A_x = A_y = A_J = A$. **a, e** Expectation value of electron x and y position in the ground state. **b, f** Orbital splitting and wavefunction projection during transfer. Blue markers indicate the time steps shown in **(d, h)**, respectively. **c, g** Corresponding applied voltage pulses. Colors follow the gate color-coding in Fig. 1. **d** First excited states for the time steps shown in **(b)**, corresponding to time steps shown in Fig. 1g. Teal, green and blue sequence correspond to the 95 %, 68 %, 1 % levels of the probability density for the first excited state. **h** Ground states and first excited states for the time steps shown in **(f)**. 95 %, 68 %, 1 % probability density levels of the ground states shown in yellow, orange and red, respectively. First excited states follow color map in **(d)**.